



Nucleation competition and phase transformation mechanisms in recycled aluminium alloys: Insights into θ -Al₁₃Fe₄, Al₆(Fe,Mn) and α -Al₁₅(Fe, Mn)₃Si₂

Zhongping Que ^{*}, Changming Fang, Zhongyun Fan

Brunel Centre for Advanced Solidification Technology (BCAST), Brunel University London, Uxbridge, Middlesex UB8 3PH, UK

ARTICLE INFO

Keywords:

Phase competition
Fe-bearing intermetallic compounds
Solidification
Phase transformation
First-principles

ABSTRACT

Aluminium rich Fe-bearing intermetallic compounds (Fe-IMCs) plays a critical role in determining the mechanical properties of recycled aluminium alloys due to inevitable Fe accumulation during recycling. The Fe-IMCs which have a needle-/plate-like morphology are particularly detrimental, impairing the ductility and overall performance of aluminium alloys. Consequently, optimizing phase selection to favour less harmful Fe-IMCs is a critical strategy for improving alloy design and enhancing material properties. The nucleation of Fe-IMCs, however, is challenging because it requires precise structural and compositional templating, involving multiple alloying elements at specific atomic positions, and thus necessitates substantial undercooling. This study examines a complicated primary phase selection among θ -Al₁₃Fe₄ and Al₆(Fe,Mn) and α -Al₁₅(Fe,Mn)₃Si₂ in an Al-5Mg-2Si-0.6Mn-1.3Fe alloy. Experimental results show θ -Al₁₃Fe₄ and Al₆(Fe,Mn) solidify as non-equilibrium primary phases ahead of the equilibrium α -Al₁₅(Fe,Mn)₃Si₂, with subsequent transformation to α -Al₁₅(Fe,Mn)₃Si₂ during later stages. Phase competition and transformation mechanisms were characterized using scanning electron microscope (SEM), electron backscatter diffraction (EBSD) and transmission electron microscope (TEM), with experimental results supported by first-principles modelling. Particular focus was given to the transition from the silicon-unfavourable Al₆(Fe,Mn) to the silicon-rich α -Al₁₅(Fe,Mn)₃Si₂. The findings provide a novel framework for designing recycled aluminium alloys with enhanced mechanical properties by optimizing Fe-IMC phase selection and transformation pathways.

1. Introduction

Full metal circularity, in which the global demand for metallic materials met by the circulation of secondary metals through reduction, reuse, remanufacture, recycling and recovery, is a vital response to this challenge [1,2]. Aluminium recycling only costs 5 % energy and reduces 95 % greenhouse gas emission compared to the primary aluminium production [3,4]. Although currently majority of aluminium scraps have been recycled, most of them were downcycled or diluted with primary aluminium [5,6]. Impurities such as Fe in the scraps are one of the most important reasons for it [7,8]. Fe, as an unavoidable impurity in current aluminium (Al) industry, plays important role in determining the mechanical properties of Al-alloys. The accumulation of Fe content from the casting and recycling process has been an urgent issue to be solved for aluminium recycling.

Due to the low solubility of Fe in the aluminium, the Fe is easily to

form the aluminium rich Fe-bearing intermetallic compounds (Fe-IMCs) with Al. The Fe-IMCs are challenging to refine or modify once the alloys have solidified. However, there are two opportunities to alter these Fe-IMCs during the manufacturing process of Al alloys. The first opportunity arises during the solidification process (casting), where initial phase formation can be influenced. It is known that the equilibrium phase diagram is hardly to predict the formation of the Fe-IMCs due to the kinetical factors and nucleation competition among different types of Fe-IMCs [9]. Understanding the complexity of Fe-IMC formation has significantly advanced over the past decade [9–13]. This progress stems from recognizing the challenges of nucleation, which necessitate both structural and compositional templating [12]. These templates require multiple alloying elements to occupy specific atomic positions, resulting in the need for significant nucleation undercooling. It has been reported that the nucleation undercoolings of different types of Fe-IMCs follows the sequence: θ -Al₁₃Fe₄ < Al₆(Fe,Mn) < α -Al₁₅(Fe,Mn)₃Si₂ [14]. This

^{*} Corresponding author.

E-mail address: Zhongping.Que@brunel.ac.uk (Z. Que).

<https://doi.org/10.1016/j.jalcom.2025.181130>

Received 10 February 2025; Received in revised form 19 May 2025; Accepted 21 May 2025

Available online 22 May 2025

0925-8388/© 2025 The Author(s). Published by Elsevier B.V. This is an open access article under the CC BY license (<http://creativecommons.org/licenses/by/4.0/>).

sequence reflects the increasing difficulty of nucleation, correlating with the number of the constitute alloying elements required. Subsequent technological advancements have demonstrated that the nucleation potency of the specific Fe-IMCs can be manipulated through composition and structural templating [12,15]. Studies revealed that pre-templating Fe and Si on the Al/(10 $\bar{1}$ 0)AlB₂ interface effectively facilitated the heterogeneous nucleation of α -Al₁₅(Fe,Mn)₃Si₂, leading to significant refinement of this compound [12].

The second opportunity is during heat treatment, which can facilitate the phase transformations and modify the morphology of small size Fe-IMCs. The composition and the crystal structure of these Al-Fe compounds are very flexible. For example, the Al-Fe compounds are easily incorporated with the other alloying elements such as Si, Mn, Cr, Ni, Co, etc. [16–20]. Different alloying elements doping in the Al-Fe intermetallic compounds (IMCs) cause the composition and the crystal structure variation [16–21]. Therefore, there are more than 20 types of Fe-IMCs reported so far. Most of the alloying elements incorporating in the Fe-IMCs by replacing the atomic position of Al or Fe, such as Si replacing the Al atoms in θ -Al₁₃Fe₄, Mn replace the Fe atoms in most of the Fe-IMCs. Recent research reported that the vanadium can also possibly incorporate into θ -Al₁₃Fe₄ by partially occupying atomic position of Al [22].

The incorporation of Si is generally facilitating phase transformations among different types of the Fe intermetallic compounds [13,23,24]. A typical example showing the phase transformation sequence from θ -Al₁₃Fe₄ to α -Al₆Fe₂Si, β -Al₅FeSi and then δ -Al₄Fe₂Si demonstrated that these phase transitions are diffusion control and the phase transition sequence follows the increasing Si concentration in these Fe-IMCs. The morphology of the Fe-IMCs can be modified due to the phase transition, which therefore benefits the mechanical properties. Recently research work [25] demonstrated the benefits of mechanical properties improvement from phase transformation between Al₆(Fe,Mn) and the α -AlFeSi during the heat treatment process, in which Si content in the crystals plays an important role. Meanwhile previous investigations on this type of phase transformation have primarily focus on describing composition and morphology and the understanding of the underlying mechanism remains limited due to the absence of an observable specific crystallography orientation relationship.

In this study, the co-selection of three different types of primary Fe-IMs including θ -Al₁₃Fe₄, Al₆(Fe,Mn), α -Al₁₅(Fe,Mn)₃Si₂ was observed during the solidification of an Al-5Mg-2Si-0.6Mn-1.3Fe alloy poured at 700 °C with a cooling rate of 3.5 K/s. The selected non-equilibrium θ -Al₁₃Fe₄, Al₆(Fe,Mn) phase transformed into equilibrium α -Al₁₅(Fe,Mn)₃Si₂ in the following solidification process. The complex competition among multiple primary Fe-IMCs will be examined using various characterization methods, ranging from SEM to crystallographic analysis. Phase transitions between θ -Al₁₃Fe₄/ α -Al₁₅(Fe,Mn)₃Si₂, θ -Al₁₃Fe₄/Al₆(Fe,Mn), and Al₆(Fe,Mn)/ α -Al₁₅(Fe,Mn)₃Si₂ are investigated by mean of a combination of experimental techniques including scanning electron microscope (SEM) and transmission electron microscope (TEM) and first-principles' modelling. Parameter-free first-principles method is employed to obtain insights into the intrinsic structural properties and energetics of related intermetallic compounds. This method provides valuable formation to understand the formation and transformation of Fe-IMCs during solidification [26–28].

2. Experimental

2.1. Casting and characterization

The nominal composition of the studied alloy is Al-5Mg-2Si-0.6Mn-1.3Fe. The actual composition of the studied alloy is 5.1 \pm 0.5Mg, 2.0 \pm 0.3 Si, 0.6 \pm 0.1 Mn and 1.3 \pm 0.05 Fe (in wt%) with Al balance. The phase diagram and the solidification curve were calculated with Pandat software [29] with Scheil model [30] and displayed in Fig. 1. The

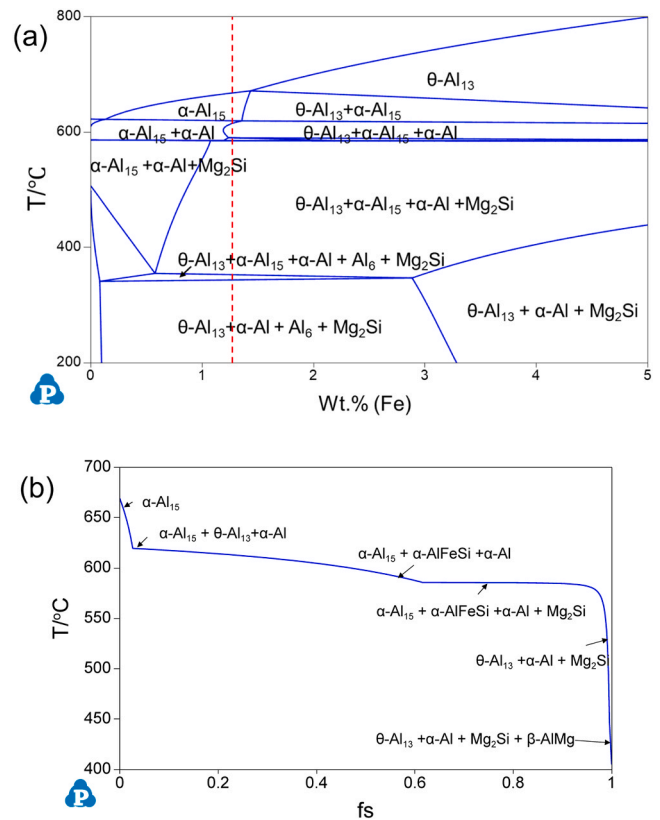


Fig. 1. (a) Calculated phase diagram of the Al-5.1Mg-2.0Si-0.6Mn-xFe alloy system, and (b) simulated solidification curve of the Al-5.1Mg-2.0Si-0.6Mn-1.3Fe alloy.

thermodynamics study showed that the solidification sequence of the studied Al-5.1Mg-2.0Si-0.6Mn-1.3Fe alloy was as: L \rightarrow α -Al₁₅(Fe,Mn)₃Si₂ (P-IMC), L \rightarrow α -Al₁₅(Fe,Mn)₃Si₂ (BE-IMC) + α -Al, and L \rightarrow α -Al₁₅(Fe,Mn)₃Si₂ (TE-IMC) + α -Al + Mg₂Si. The calculated liquidus is 668.7 °C. The composition of the studied alloy is very close to the threshold required for solidification with primary θ -Al₁₃Fe₄. However, it is significantly different from the composition needed for solidification with primary Al₆(Fe,Mn). Commercially pure Al (>99.8 wt%), commercially pure (CP) Mg (>99.95 wt%), and master alloys of Al-50 wt% Si, Al-20 wt% Mn, and Al-38 wt% Fe were utilized for the castings. The vaporization of certain alloying elements, such as Mg, was taken into account, and an additional amount of master alloys was added to ensure the actual composition closely matched the nominal alloy composition. The CP-Al samples were melted at 750°C in electric resistance furnace. Subsequently, the other master alloys, excluding CP-Mg, were added to the Al melt and stirred thoroughly to ensure complete dissolution. At last, CP-Mg wrapped in a thin Al foil preheated to 200°C, was added to the melt. Once the Mg had completely melted, the melts were held for further 30 minutes. After removing the slag, the melt was cast into a Tp-1 mould preheated to 380 °C. The Tp-1 mould is specifically designed to provide a cooling rate of 3.5 K/s at the sample section 38 mm from the bottom, which is comparable to the cooling rate of directional chilled casting [31]. The pouring temperature is 700°C.

A phase competition between primary θ -Al₁₃Fe₄ and α -Al₁₅(Fe,Mn)₃Si₂ of this studied alloy, when casted at 720°C with a cooling rate of 3.5 K/s, has been reported in previous study [13]. The nucleation competition and the subsequent phase transformation, as well as the related transition mechanism between non-equilibrium θ -Al₁₃Fe₄ and equilibrium α -Al₁₅(Fe,Mn)₃Si₂, have been clearly investigated. In this study, an even complex phase competition among three different primary Fe-IMCs: Al₆(Fe,Mn), θ -Al₁₃Fe₄ and α -Al₁₅(Fe,Mn)₃Si₂, will be presented, and the subsequent phase transformation, among these three

different phases will be further examined. Multiple influencing factors, such as cooling rate, nucleation undercooling, elemental diffusion and composition segregation, and the relationship between composition, lattice parameters, and crystallography, will be investigated to explain the mechanism of this complex nucleation competition and phase transformation.

Metallographic specimens were prepared using the standard procedures. The as-cast microstructure characteristics of the samples were examined using a Zeiss optical microscope fitted with the Axio Vision 4.3 image analysis software. The electron backscatter diffraction (EBSD) technique was applied for phase identification and examining the phase relationships among the solidified Fe-IMCs in Al-5Mg-2Si-0.6Mn-1.3Fe alloy. The scanning step size was 0.1–0.5 μm . To observe the 3-dimensional (3D) morphology of intermetallic compounds in this study, the as-cast samples were deep etched in 15 % HCl solution for 2–3 minutes followed the methanol bath. The EBSD and SEM investigation were made on a Zeiss Cross beam 340 FIB-SEM operated at an accelerating voltage of 20 kV. To investigate the interface between different Fe-IMCs, the transmission electron microscopy (TEM) sample was prepared with focused ion beam (FIB) on the Zeiss Cross beam 340 FIB-SEM. TEM examination was performed on a JEOL 2100 F transmission electron microscope equipped with EDX spectrometer operated at an accelerating voltage of 200 kV.

2.2. Computational methods

The first-principles Vienna *Ab initio* Simulation Package (VASP) [32] was utilized for the calculations in this work. VASP uses the density-functional theory within the projector-augmented wave (PAW) method [33]. The (spin-polarized) generalized gradient approximation was employed for the exchange and correlation energy terms [34]. The cut-off energy of the wave functions was set to be 550 eV and the cut-off energy of the augmentation functions was set to be 700 eV. The electronic wave functions were sampled on dense grids in the irreducible Brillouin zone (BZ) of the systems. Structural optimizations were performed for both lattice parameters and coordinates of atoms. Different k -meshes and cut-off energies were tested for the waves and augmentation waves, respectively. Tests showed a good convergence (<1 meV per atom).

3. Results

3.1. Heterogeneous nucleation competition among $\text{Al}_6(\text{Fe,Mn})$, $\theta\text{-Al}_{13}\text{Fe}_4$ and $\alpha\text{-Al}_{15}(\text{Fe,Mn})_3\text{Si}_2$

Fig. 2 shows the SEM-BSD images of the as-cast microstructure of Al-5Mg-2Si-0.6Mn-1.3Fe cast at 700 °C with a cooling rate of 3.5 K/s, illustrating the complex phase selection among multiple Fe-bearing intermetallic compounds. Three different types of Fe-IMCs with distinct morphologies can be easily recognized in Fig. 2a. The predominant Fe-IMC, exhibiting a Chinese script morphology, is identified as $\alpha\text{-Al}_{15}(\text{Fe,Mn})_3\text{Si}_2$, confirmed later through EBSD and TEM analysis. The average composition of $\alpha\text{-Al}_{15}(\text{Fe,Mn})_3\text{Si}_2$ is found to be 5.7 at% Si, 10.2 at% Fe and 4.6 at% Mn. The plate-like Fe-IMC (minor phase) is identified as $\theta\text{-Al}_{13}\text{Fe}_4$ later with EBSD. A small amount of Si (2.6 at%) and Mn (2.2 at%) are incorporated into $\theta\text{-Al}_{13}\text{Fe}_4$, but the crystal structure remains unchanged. A few Fe-IMCs particles with coarse branch spacing and a Chinese script morphology were identified as $\text{Al}_6(\text{Fe,Mn})$ later through EBSD and TEM analysis. Unlike the other Fe-IMCs, no Si was detected in $\text{Al}_6(\text{Fe,Mn})$, which is a distinctive characteristic of this phase. Notably, the majority of $\text{Al}_6(\text{Fe,Mn})$ particles solidified at the very edge of the sample, where the cooling rate is higher, as shown in Fig. 2b. Fig. 2c reveals that the $\text{Al}_6(\text{Fe,Mn})$ exhibit a hollow morphology, which corresponds to the structure reported in [35].

Further SEM investigation shows that three different types of primary Fe-IMCs: $\alpha\text{-Al}_{15}(\text{Fe,Mn})_3\text{Si}_2$, $\text{Al}_6(\text{Fe,Mn})$ and $\theta\text{-Al}_{13}\text{Fe}_4$ can solidify

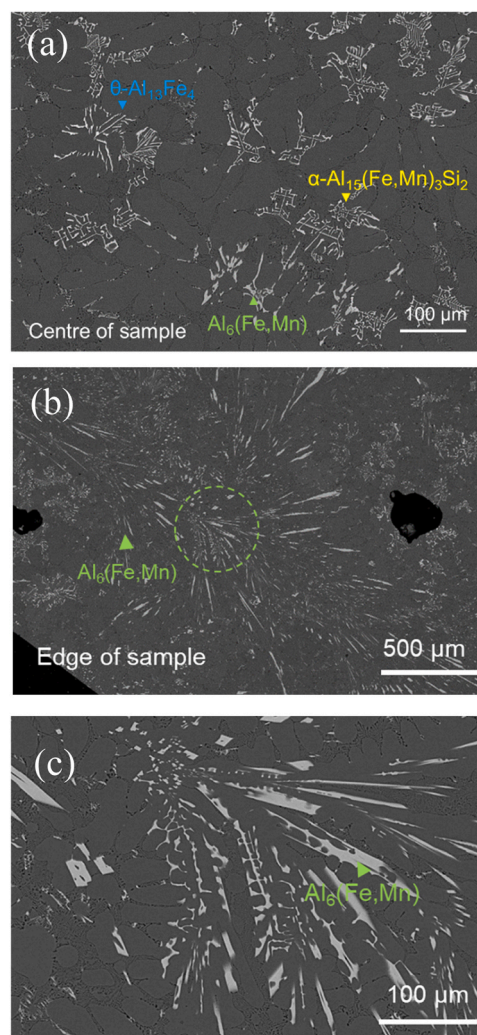


Fig. 2. SEM-BSD images of the as-cast microstructure of Al-5Mg-2Si-0.6Mn-1.3Fe cast at 700 °C with a cooling rate of 3.5 K/s, showing the multiple phase selection of Fe-bearing intermetallic compounds. (a) Central region of the sample showing predominant $\alpha\text{-Al}_{15}(\text{Fe,Mn})_3\text{Si}_2$ with Chinese script morphology, minor $\theta\text{-Al}_{13}\text{Fe}_4$ with needle/plate-like morphology, and trace $\text{Al}_6(\text{Fe,Mn})$ with hollowed Chinese script morphology. (b) Edge region of the sample showing dominant $\text{Al}_6(\text{Fe,Mn})$ with hollowed Chinese script morphology and $\alpha\text{-Al}_{15}(\text{Fe,Mn})_3\text{Si}_2$ with Chinese script morphology. (c) Magnified view of the $\text{Al}_6(\text{Fe,Mn})$ from the green dotted area in (b), revealing its hollowed Chinese script morphology.

and initiate the formation of the same Fe-IMCs in the subsequent binary eutectic. The results are shown in Fig. 3. Fig. 3a shows that the compact $\alpha\text{-Al}_{15}(\text{Fe,Mn})_3\text{Si}_2$ nucleates the binary eutectic $\alpha\text{-Al}_{15}(\text{Fe,Mn})_3\text{Si}_2$ with Chinese script morphology. Fig. 3b reveals that the hollowed $\text{Al}_6(\text{Fe,Mn})$ needles nucleate the binary eutectic ($\text{Al}_6(\text{Fe,Mn}) + \alpha\text{-Al}$), also exhibiting a Chinese script/hollow morphology. Fig. 3c presents that the plate-like $\theta\text{-Al}_{13}\text{Fe}_4$ nucleates the binary eutectic ($\theta\text{-Al}_{13}\text{Fe}_4 + \alpha\text{-Al}$), maintaining a plate-like morphology.

3.2. Phase transformation between $\text{Al}_6(\text{Fe,Mn})/\theta\text{-Al}_{13}\text{Fe}_4$, $\theta\text{-Al}_{13}\text{Fe}_4/\alpha\text{-Al}_{15}(\text{Fe,Mn})_3\text{Si}_2$ and $\text{Al}_6(\text{Fe,Mn})/\alpha\text{-Al}_{15}(\text{Fe,Mn})_3\text{Si}_2$

However, upon closer examination, several phase transformations between these Fe-IMCs were observed. Fig. 4a shows that the compacted primary $\alpha\text{-Al}_{15}(\text{Fe,Mn})_3\text{Si}_2$ has actually transformed from primary $\theta\text{-Al}_{13}\text{Fe}_4$. Fig. 4b displays that the plate-like primary θ has transformed into α at the surface, thereby nucleating the Chinese script binary

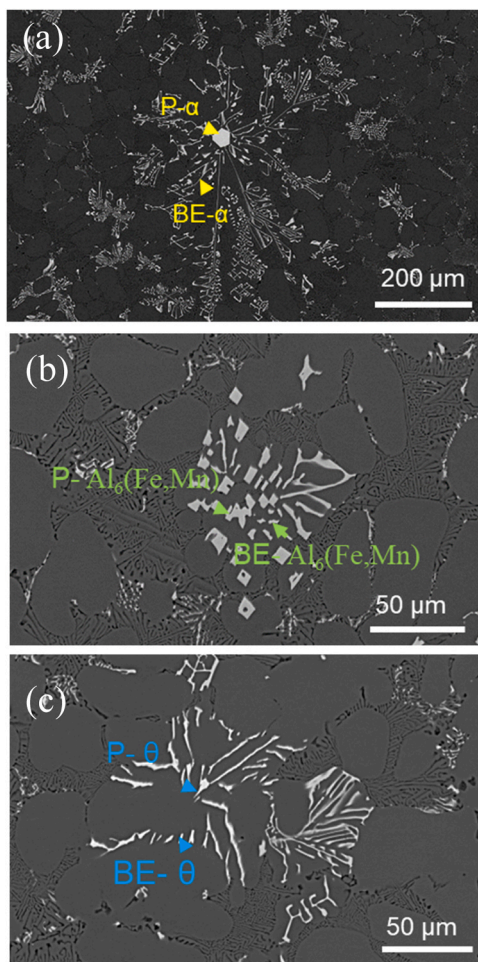


Fig. 3. SEM-BSD images of the as-cast microstructure of Al-5Mg-2Si-0.6Mn-1.3Fe alloy cast at 700 °C with a cooling rate of 3.5 K/s, showing that each type of selected primary Fe-containing compounds can serve as a nucleation site for the same phase in the following solidified binary eutectic (BE) structure. (a) Primary α -Al₁₅(Fe,Mn)₃Si₂ with a compact morphology nucleating Chinese script BE- α -Al₁₅(Fe,Mn)₃Si₂. (b) Hollowed primary Al₆(Fe,Mn) nucleated the Chinese script Al₆(Fe,Mn). (c) Needle-/plate-like primary θ -Al₁₃Fe₄ initiating the formation of θ -Al₁₃Fe₄ in the binary eutectic. (Note: α denotes α -Al₁₅(Fe, Mn)₃Si₂, θ represents θ -Al₁₃Fe₄).

eutectic- α . Fig. 4c presents that the solidified primary Al₆(Fe,Mn) has transformed into a double-phase structure of α -Al₁₅(Fe,Mn)₃Si₂ and α -Al, which subsequently nucleated the binary eutectic α -Al₁₅(Fe, Mn)₃Si₂.

The 3D morphology of these characterizations is presented in Fig. 5. Fig. 5a demonstrates that when small-sized θ particles transform into α and are fully covered by α particles, the phase transformation phenomenon is easily to be covered without careful observation. The details of this challenge have been well explained in our previous publication with SEM, EBSD and CT analyses [13]. This highlights the challenge in understanding the difficulty of the formation of Fe-IMCs. Fig. 5b shows the typical plate-like structure of the θ phase, with tiny steps/defaults on the plates. Some α -Al₁₅(Fe,Mn)₃Si₂ particles can be observed to nucleate on these plates, likely due to the phase transformation from θ to α occurring on these surfaces. Fig. 5c presents Al₆(Fe,Mn) needles that have transformed into α -Al₁₅(Fe,Mn)₃Si₂ and α -Al double phases at the surface, which then nucleated the following binary α -Al₁₅(Fe,Mn)₃Si₂.

Fig. 2b shows that at the edge of the Tp-1 sample, Al₆(Fe,Mn) solidifies as the dominating Fe-IMC. The potential phase transformation in these Al₆(Fe,Mn) rich area was investigated using EBSD mapping, shown in Fig. 6. The phase mapping in Fig. 6b reveals two different types of

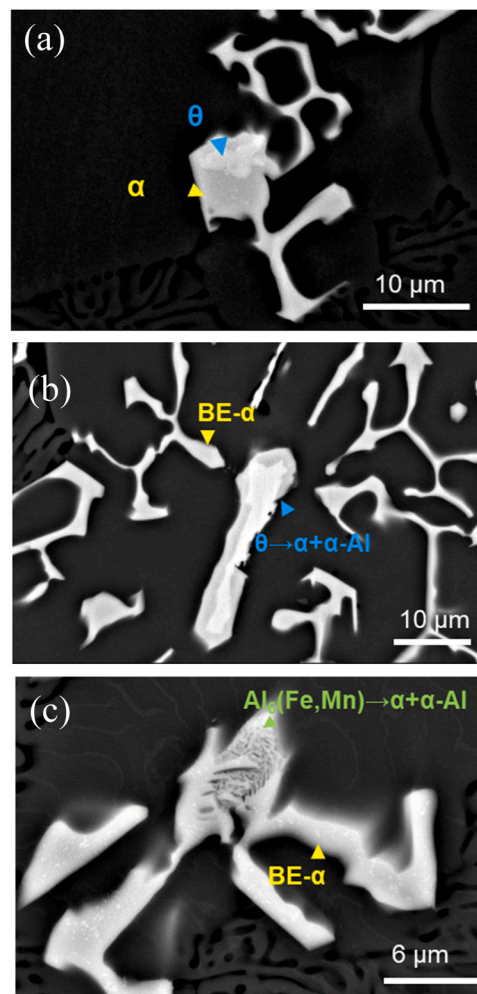


Fig. 4. SEM-BSD images of the as-cast microstructure of Al-5Mg-2Si-0.6Mn-1.3Fe cast at 700 °C with a cooling rate of 3.5 K/s, showing transformation pathways of primary Fe-IMCs and their role in eutectic nucleation. (a) Primary θ -Al₁₃Fe₄ transformed into compact primary α -Al₁₅(Fe,Mn)₃Si₂ which subsequently nucleated the binary eutectic α -Al₁₅(Fe,Mn)₃Si₂. (b) Needle/plate-like θ -Al₁₃Fe₄ partially transformed at the surface into α -Al₁₅(Fe,Mn)₃Si₂ and acted as a nucleation site for the eutectic α -Al₁₅(Fe,Mn)₃Si₂. (c) Primary Al₆(Fe, Mn) transformed into a dual-phase region comprising α -Al₁₅(Fe,Mn)₃Si₂ and α -Al, and served as the nucleation site for the eutectic α -Al₁₅(Fe,Mn)₃Si₂.

phase transition: Al₆(Fe,Mn) (pink) to α -Al₁₅(Fe,Mn)₃Si₂ (green), and Al₆(Fe,Mn) (pink) to θ -Al₁₃Fe₄ (blue). A portion of the Al₆(Fe,Mn) remains untransformed.

However, compared to the distinct phase transition characterization between Al₆(Fe,Mn) and α -Al₁₅(Fe,Mn)₃Si₂ (Figs. 4c and 5c), the phase transformation between Al₆(Fe,Mn) and θ -Al₁₃Fe₄ is less apparent and difficult to observe under SEM. The Al₆(Fe,Mn) particle identified for the Al₆(Fe,Mn)/ θ -Al₁₃Fe₄ phase transition in Fig. 6b was re-examined with SEM, and the results are shown in Fig. 7. Fig. 7a shows no visible phase transformation characterization, like that observed between Al₆(Fe,Mn) and α -Al₁₅(Fe,Mn)₃Si₂. However, the SEM-line scanning spectrum in Fig. 7b reveals a composition variation from left to right, with increasing Fe, decreasing Mn and no or very small increases in Si concentration. The composition of different types of Fe-IMC in this study, shown in Table 1, reveals that, compared to Al₆(Fe,Mn), θ -Al₁₃Fe₄ has a much higher Fe concentration, lower Mn and can incorporate up to 2.6 at% Si. The examination results from the EBSD mapping (Fig. 5) and the SEM-EDS line scanning (Fig. 7) demonstrate that phase transition from Al₆(Fe,Mn) to θ -Al₁₃Fe₄ happened.

The phase transitions between Al₆(Fe,Mn)/ α -Al₁₅(Fe,Mn)₃Si₂, and

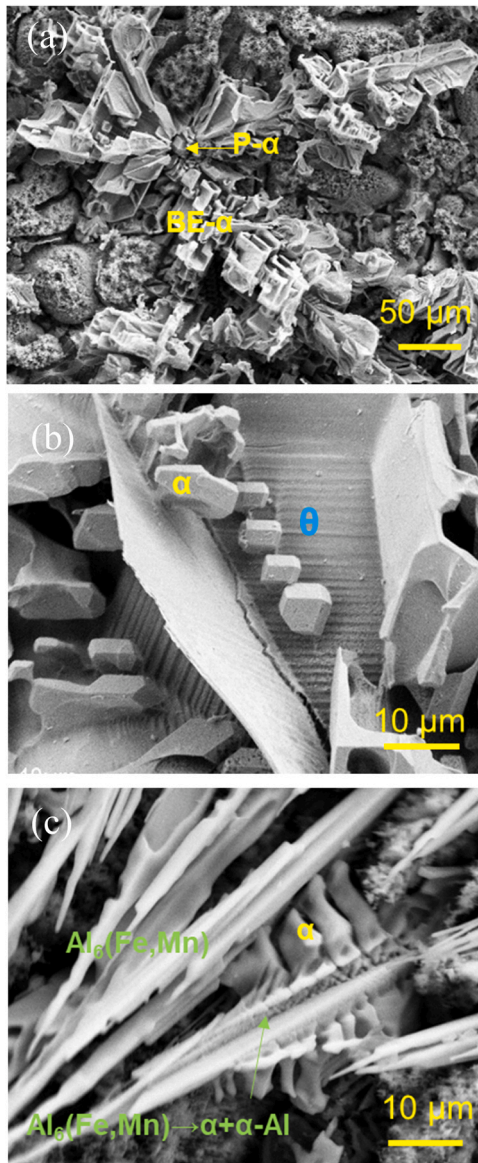


Fig. 5. SEM images of the as-cast microstructure of Al-5Mg-2Si-0.6Mn-1.3Fe alloy cast at 700 °C with a cooling rate of 3.5 K/s, showing the 3-dimensional (3D) morphology and interconnectivity of Fe-IMCs. (a) Primary α -Al₁₅(Fe, Mn)₃Si₂ particle connected to eutectic α -Al₁₅(Fe, Mn)₃Si₂ with Chinese script. (b) Plate-like θ -Al₁₃Fe₄ with stepped surfaces connected to compact/Chinese script α -Al₁₅(Fe, Mn)₃Si₂. (c) Hollow needle-like Al₆(Fe, Mn) exhibiting surface phase transition and connect to Chinese script α -Al₁₅(Fe, Mn)₃Si₂.

θ -Al₁₃Fe₄/ α -Al₁₅(Fe, Mn)₃Si₂ were compared under SEM-BSD examination, as shown in Fig. 8. Fig. 8a shows that the primary Al₆(Fe, Mn) particle transformed into α -Al₁₅(Fe, Mn)₃Si₂ and α -Al double phases at the surface, while the shape of the original Al₆(Fe, Mn) particle remains unchanged. Notably, the transformed double phases exhibit a lamellar morphology rather than the randomly distributed, nano-sized, or rod-like structures reported in [23,24]. The lamellar plates are aligned perpendicular to the interface (orange frame). The phase transformation can be defined as:

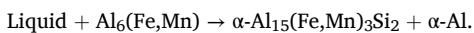


Fig. 8b shows that the θ -Al₁₃Fe₄ transformed into α -Al₁₅(Fe, Mn)₃Si₂ but retained its original size. No lamellar morphology can be observed in this transformed structure. Instead, a few randomly distributed α -Al dots are seen within the transformed α -Al₁₅(Fe, Mn)₃Si₂. The phase

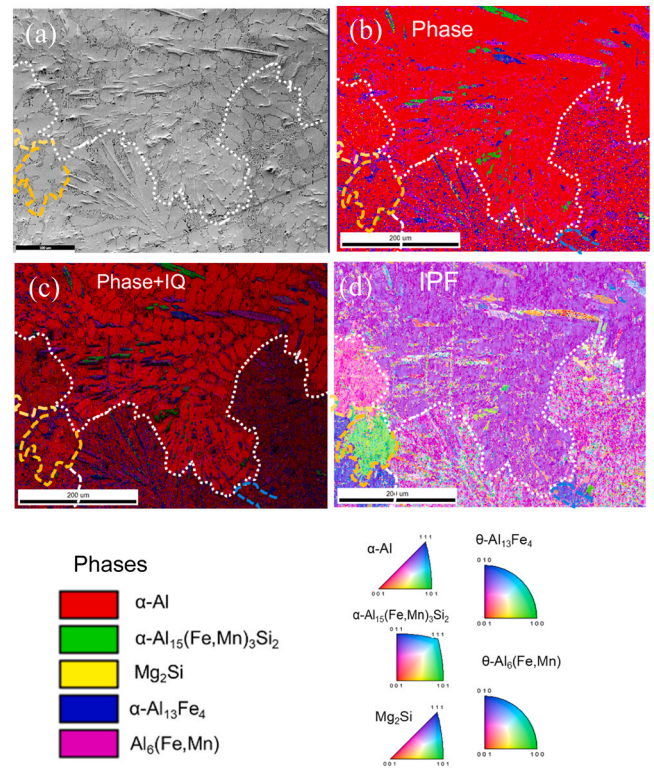
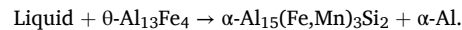


Fig. 6. The EBSD mapping of the Al₆(Fe, Mn)-rich area located at the edge of the TP-1 sample, showing two different types of phase transition: Al₆(Fe, Mn) → α -Al₁₅(Fe, Mn)₃Si₂, and Al₆(Fe, Mn) → θ -Al₁₃Fe₄. (a) SEM image of the mapped area. (b) Phase map identifying the constituent intermetallic phases. (c) Phase map overlaid with image quality (IQ) contrast, and (d) inverse pole figure (IPF) map.

transformation can be defined as:



Details on the phase transformation between θ -Al₁₃Fe₄ and α -Al₁₅(Fe, Mn)₃Si₂ have been reported previously [13]. Therefore, this study will focus on the phase transformation between Al₆(Fe, Mn) and α -Al₁₅(Fe, Mn)₃Si₂.

3.3. Nature of phase transformation from Si-free Al₆(Fe, Mn) to Si-rich α -Al₁₅(Fe, Mn)₃Si₂

The interface of the phase formation between Al₆(Fe, Mn) and α -Al₁₅(Fe, Mn)₃Si₂ were examined using TEM, and the results are shown in Fig. 9. Fig. 9a presents the bright field TEM image of a FIB sample, showing the interface between the Al₆(Fe, Mn) and the transformed lamellar structure consisting of α -Al₁₅(Fe, Mn)₃Si₂ and α -Al. The selected area electron diffraction (SAED) patterns for α -Al₁₅(Fe, Mn)₃Si₂, Al₆(Fe, Mn) and α -Al, viewed along their low zone directions, are displayed in Fig. 9b, c and d. To investigate the orientation relationship between Al₆(Fe, Mn) and α -Al₁₅(Fe, Mn)₃Si₂, these two Fe-IMCs were carefully examined along different zone axes within the limitations of TEM operation (α and β tilt angles). No specific orientation relationship could be found between Al₆(Fe, Mn) and α -Al₁₅(Fe, Mn)₃Si₂, which is different to the other types of phase transformation between Fe-IMCs [23,24].

The interface between α -Al₁₅(Fe, Mn)₃Si₂ and α -Al was also investigated using TEM. The results are shown in Fig. 10. Fig. 10a is the bright field TEM image displaying the interface between the transformed lamellar α -Al₁₅(Fe, Mn)₃Si₂ and α -Al when α -Al₁₅(Fe, Mn)₃Si₂ is viewed along the [1 0 0] zone direction. Fig. 10b shows the absence of a specific orientation relationship between α -Al₁₅(Fe, Mn)₃Si₂ and α -Al. Although

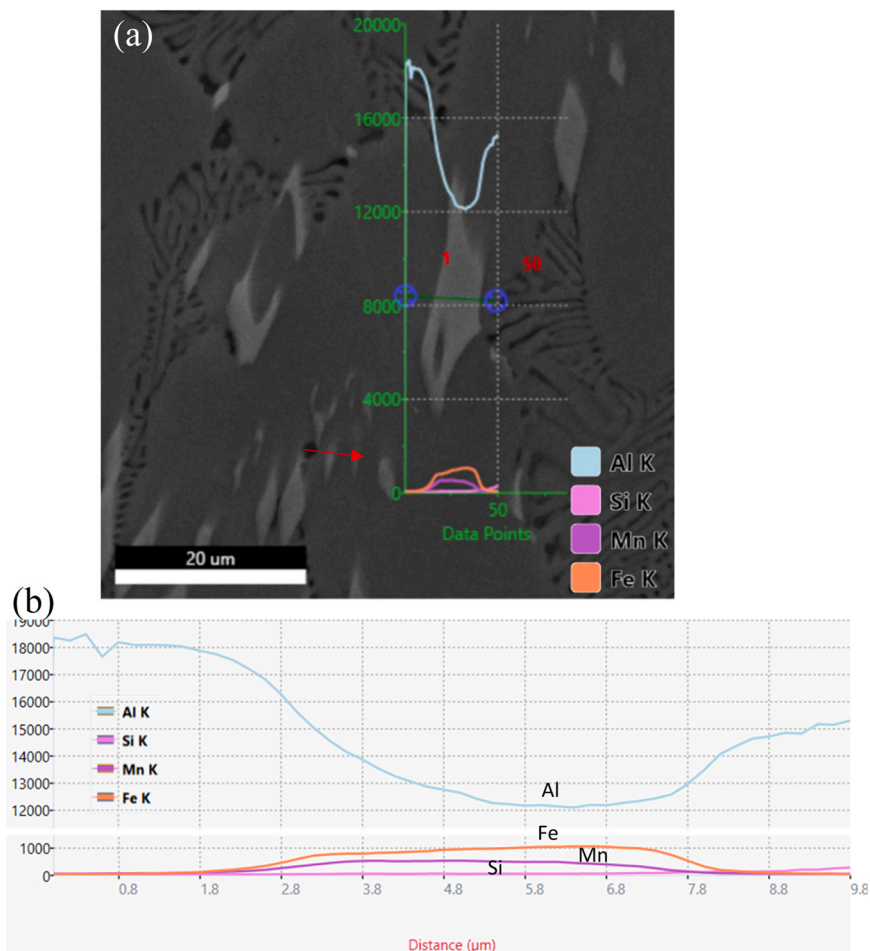


Fig. 7. (a) SEM line scan across a hollowed $\text{Al}_6(\text{Fe,Mn})$ particle showing compositional variation, and (b) corresponding EDS spectrum profile from left to right, showing an increase in Fe content and a decrease in Mn content along the scan path.

Table 1

The average composition (at%) of different types of Fe-IMCs in this study.

Fe-IMCs		Al	Fe	Mn	Si
$\text{Al}_6(\text{Fe,Mn})$	SEM-EDS	86.48 ± 0.5	9.27 ± 0.4	4.25 ± 0.2	ND (non-detected)
	TEM-EDS	88.87 ± 0.4	7.42 ± 0.3	3.73 ± 0.2	ND
Primary $\alpha\text{-Al}_{15}(\text{Fe,Mn})_3\text{Si}_2$	TEM-EDS	79.5 ± 0.6	10.2 ± 0.5	4.6 ± 0.2	5.7 ± 0.2
	Binary eutectic $\alpha\text{-Al}_{15}(\text{Fe,Mn})_3\text{Si}_2$	TEM-EDS	79.1 ± 0.4	8.9 ± 0.4	5.7 ± 0.2
Ternary eutectic $\alpha\text{-Al}_{15}(\text{Fe,Mn})_3\text{Si}_2$	TEM-EDS	84.95 ± 0.4	13.1 ± 0.5	0.75 ± 0.0	1.2 ± 0.05
	$\theta\text{-Al}_{13}\text{Fe}_4$	TEM-EDS	78.6 ± 0.4	18.7 ± 0.5	2.2 ± 0.1

$\alpha\text{-Al}_{15}(\text{Fe,Mn})_3\text{Si}_2$ is typically reported as (1 1 0) faceted intermetallic compound [36], in this samples, no faceted surface can be observed at between the $\alpha\text{-Al}_{15}(\text{Fe,Mn})_3\text{Si}_2$ and $\alpha\text{-Al}$, instead of some diffusion trace observed at the interface as shown in Fig. 10b. The $\alpha\text{-Al}$ was then tilted and further investigated under different zone directions, but still, no specific orientation relationship between $\alpha\text{-Al}_{15}(\text{Fe,Mn})_3\text{Si}_2$ and $\alpha\text{-Al}$ could be found. Additionally, when viewed along the [1 1 0] zone direction of $\alpha\text{-Al}$, some needle-like precipitates were observed in the $\alpha\text{-Al}$ originating from the lamellar structure (Fig. 10c). These precipitates may be the result of solutes rejected during the phase transformation

between $\text{Al}_6(\text{Fe,Mn})$ and $\alpha\text{-Al}_{15}(\text{Fe,Mn})_3\text{Si}_2$, balancing the composition at the interface.

3.4. Computational results on the stability of $\text{Al}_6(\text{Fe, Mn})$, $\theta\text{-Al}_{13}\text{Fe}_4$ and $\alpha\text{-Al}_{15}(\text{Fe, Mn})_3\text{Si}_2$

To assess the relative stability of different Fe-IMCs, the formation energy (ΔE_f) per M (M = Fe or Mn) atom of $(\text{Al}_{1-x}\text{Si}_x)_z(\text{Fe}_{1-y}\text{Mn}_y)$ is defined by the following equation:

$$\Delta E_f = E\{(\text{Al}_{1-x}\text{Si}_x)_z(\text{Fe}_{1-y}\text{Mn}_y)\} - \{z[(1-x)E(\text{Al}) + xE(\text{Si})] + (1-y)E(\text{Fe}^*) + yE(\text{Mn}^*)\} \quad (1)$$

Here, x, y, z are compositional parameters, representing the fraction of Si, Mn and Fe in the intermetallic compound in relation to the elemental solids ($\alpha\text{-Al}$ and Si) and solute solution of Fe, Mn in Al matrix. Equ. 1 also indicated that the impurity Si solution at the Al sublattice and Mn at the Fe sublattice, respectively.

Here, $E\{(\text{Al}_{1-x}\text{Si}_x)_z(\text{Fe}_{1-y}\text{Mn}_y)\}$, $E(\text{Al})$, $E(\text{Si})$, $E(\text{Fe}^*)$ and $E(\text{Mn}^*)$ represent the calculated total-valence electron energies for $(\text{Al}_{1-x}\text{Si}_x)_z(\text{Fe}_{1-y}\text{Mn}_y)$, elemental Al, Si, and the dilute solution energy of Fe and Mn in the Al matrix. A negative value of ΔE_f indicates that the formation of $(\text{Al}_{1-x}\text{Si}_x)_z(\text{Fe}_{1-y}\text{Mn}_y)$ is favoured. The unit of ΔE_f is eV/M (M = $\text{Fe}_{1-x}\text{Mn}_x$). At temperature $T = 0$ K and pressure $p = 0$ Pa, the enthalpy difference is equal to the energy difference, e.g. $\Delta H = \Delta E_f$, when the zero-point vibration contribution is neglected.

First-principles' calculations were firstly performed for the dilute solution of Mn, Fe and Si in the Al matrix. A supercell of $3a_0 \times 3a_0 \times 3a_0$

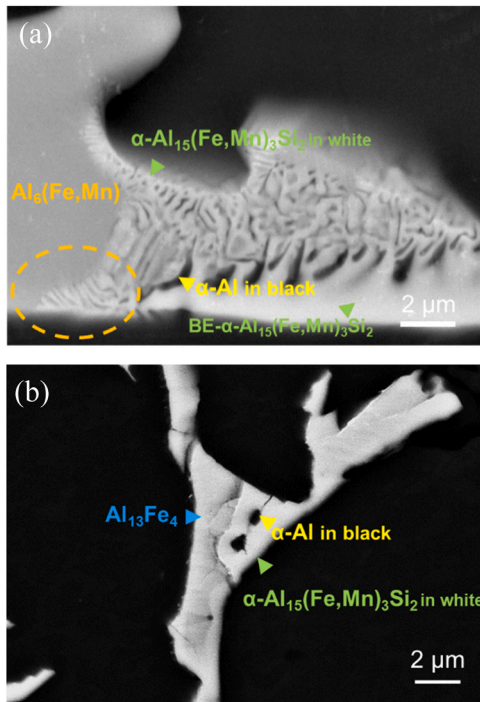


Fig. 8. SEM-BSD images showing the phase transformation behaviour of primary Fe-IMCs. (a) A primary $\text{Al}_6(\text{Fe,Mn})$ particle transforming at the surface into a dual-phase region of $\alpha\text{-Al}_{15}(\text{Fe,Mn})_3\text{Si}_2$ and $\alpha\text{-Al}$. The transformed phases exhibit a lamellar morphology, with plates oriented perpendicular to the interface (highlighted by the orange frame), and (b) $\theta\text{-Al}_{13}\text{Fe}_4$ transforming into $\alpha\text{-Al}_{15}(\text{Fe,Mn})_3\text{Si}_2$ while largely retaining its original size, with only a few $\alpha\text{-Al}$ dots embedded within the newly formed $\alpha\text{-Al}_{15}(\text{Fe,Mn})_3\text{Si}_2$.

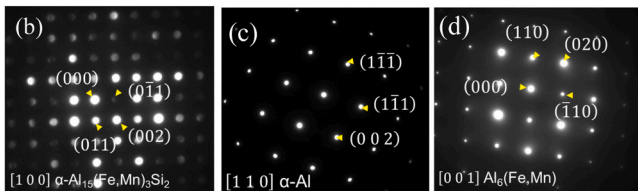
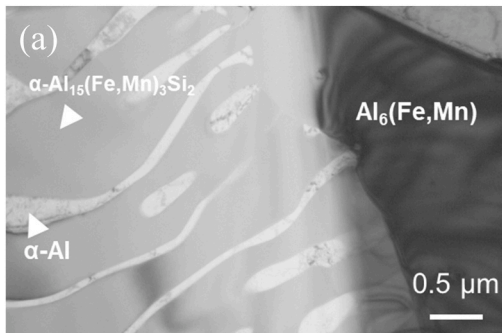


Fig. 9. (a) Bright field TEM image from a FIB-prepared sample showing the interface between primary $\text{Al}_6(\text{Fe,Mn})$ and the transited lamellar ($\alpha\text{-Al}_{15}(\text{Fe,Mn})_3\text{Si}_2 + \alpha\text{-Al}$). Selected area electron diffraction (SAED) patterns obtained from: (b) $\alpha\text{-Al}_{15}(\text{Fe,Mn})_3\text{Si}_2$ with the incident electron beam aligned along the [1 0 0] zone axis, (c) $\alpha\text{-Al}$ with the incident electron beam aligned along the [1 1 0] zone axis, and (d) $\text{Al}_6(\text{Fe,Mn})$ with the incident electron beam aligned along the [0 0 1] zone axis.

(where a_0 is the lattice parameter of Al) was employed for these calculations. The calculated solution energy, $\Delta E(M^*)$, for Fe, Mn and Si solution in Al were -0.266 eV/M, -0.348 eV/M and 0.431 eV/M, respectively. These values are in good agreement with previous

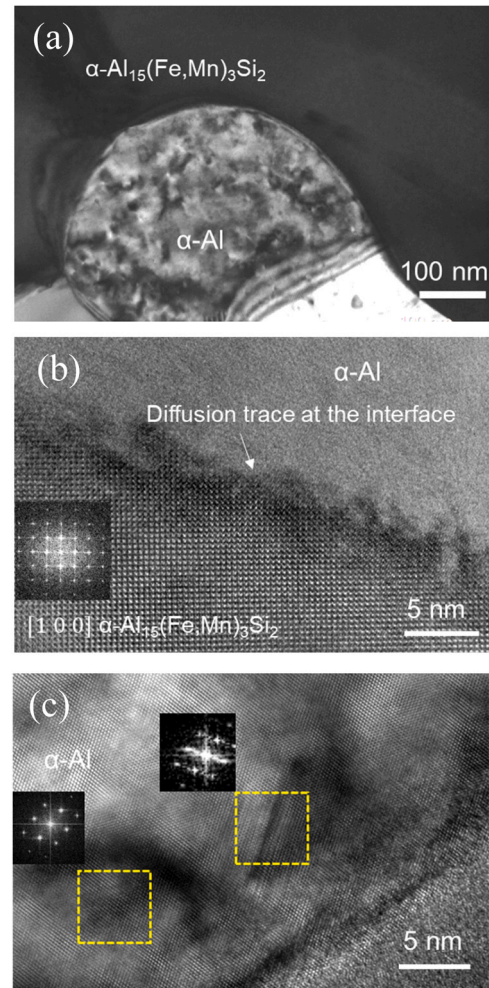


Fig. 10. (a) Bright field TEM image showing the interface between the transformed lamellar $\alpha\text{-Al}_{15}(\text{Fe,Mn})_3\text{Si}_2$ and $\alpha\text{-Al}$ phases. (b) High-resolution TEM (HRTEM) image of the $\alpha\text{-Al}_{15}(\text{Fe,Mn})_3\text{Si}_2 / \alpha\text{-Al}$ interface, viewed along the [1 0 0] zone axis of $\alpha\text{-Al}_{15}(\text{Fe,Mn})_3\text{Si}_2$, revealing diffusion features at the interface. (c) HRTEM image of needle-like precipitate within the $\alpha\text{-Al}$ matrix, viewed along the [1 1 0] zone axis, along with corresponding fast Fourier transformation (FFT) patterns from both the $\alpha\text{-Al}$ and the needle-like phase.

calculations [33,34] using the same approach. The high energy cost of Si solution in Al, caused usage of the bulk Si energy as the reference in Equ. 1.

A. Si stabilizes the $\alpha\text{-Al}_{15}(\text{Fe, Mn})_3\text{Si}_2$ phase

The structural model of $\alpha\text{-Al}_{15}(\text{Fe, Mn})_3\text{Si}_2$ phase was proposed by Cooper in 1967 [37], building upon their earlier work on the $\alpha\text{-Al}_{15}(\text{Fe, Mn})_3\text{Si}_2$ phase [38]. This phase consists of 11 different atomic species, including two types of transition metals and nine types of Al(Si) atoms, with the chemical formula $(\text{Al,Si})_{114}(\text{Fe, Mn})_{24}$. In Cooper's model, an averaged mixing of Fe/Mn atoms was assumed, although no specific discussion regarding the distribution of Si atoms was provided [37]. This structural model has been widely used for analysis of the cubic $\alpha\text{-Al}_{15}(\text{Fe, Mn})_3\text{Si}_2$ phase. Therefore, the space group $\text{Pm}\bar{3}$ used in the Cooper model represented the 'averaged' structure. In practice, Al/Si or Fe/Mn mixing caused symmetry broken of the systems.

Based on the Cooper model and the current experimental results, we firstly investigated the distribution of Mn within the α phase for the assumed $\text{Al}_{4.75}(\text{Fe}_{2/3}\text{Mn}_{1/3})$ composition. The computational analysis revealed that the formation energies associated with Mn occupying various Fe sites, as per Cooper's notation [37], are

moderate. The calculated lattice parameters and formation energy for $\alpha\text{-Al}_{4.75}(\text{Fe}_{2/3}\text{Mn}_{1/3})$ are displayed in Table 3. Notably, the computed formation energy for the Si-free $\alpha\text{-Al}_{4.75}(\text{Fe}_{2/3}\text{Mn}_{1/3})$ phase is -877 meV/M.

Structural modelling was conducted for configurations with varying Si contents at the different Al sites. The calculations demonstrated that the α phase with the experimental composition, $(\text{Al}_{0.94}\text{Si}_{0.06})_{4.75}(\text{Fe}_{2/3}\text{Mn}_{1/3})$ (Table 1), exhibits the highest stability, with Si partially occupying the Al4 and Al7 sites in Cooper's notation [37]. It is also notable that the experimentally observed chemical composition is notably different from that in the formula, indicating variation of the chemical composition of this phase on preparation conditions. The formation energy of this configuration is -939 meV/M, significantly lower than that of the Si-free $\alpha\text{-Al}_{4.75}(\text{Fe}_{2/3}\text{Mn}_{1/3})$ phase (-877 meV/M). This result indicates that Si stabilizes the $\alpha\text{-Al}_{15}(\text{Fe}, \text{Mn})_3\text{Si}_2$ phase.

B. The potency for Si doping in $\text{Al}_6(\text{Fe}, \text{Mn})$

A previous study reported that the formation energy and lattice parameters of the $\text{Al}_6(\text{Fe}, \text{Mn})$ phase exhibited moderate changes with increasing Mn content [26]. In the present work, calculations were performed for $\text{Al}_6(\text{Fe}_{0.6875}\text{Mn}_{0.3125})$ using a $2a_0 \times 2b_0 \times c_0$ supercell, where a_0 , b_0 and c_0 represent the lattice parameters of the conventional cell. This formulation closely aligns with the experimental composition (Table 1). The calculated results, including lattice parameters and formation energy, are presented in Table 3 alongside two related compositions ($x(\text{Mn}) = 0.25$ and $x(\text{Mn}) = 0.50$) for comparison.

The calculated formation energy of $\text{Al}_6(\text{Fe}_{0.6875}\text{Mn}_{0.3125})$ according to Equ. 1 is -919 meV/M, where M represents $\text{Fe}_{1-x}\text{Mn}_x$. This energy lies between those of the two neighbouring compositions. Additionally, the calculations yielded a formation energy of 918 meV/M for $\text{Al}_6(\text{Fe}_{2/3}\text{Mn}_{1/3})$, which was used for comparison with the cubic $\alpha\text{-Al}_{15}(\text{Fe}, \text{Mn})_3\text{Si}_2$ phase. The results are consistent with those reported in the previous study [26].

Calculations were also performed to evaluate Si incorporation at the Al sites in $\text{Al}_6(\text{Fe}_{0.6875}\text{Mn}_{0.3125})$. The results indicated a high energy cost (greater than 0.28 eV) for substituting a single Al atom with Si in this phase. This finding suggests that Si incorporation in $\text{Al}_6(\text{Fe}, \text{Mn})$ is unlikely due to the significant energy penalty associated with such substitution.

Overall, the calculations revealed that the formation energy of $\text{Al}_6(\text{Fe}_{2/3}\text{Mn}_{1/3})$ (-0.918 eV/M) is lower than that of the Si-free $\alpha\text{-Al}_{4.75}(\text{Fe}_{2/3}\text{Mn}_{1/3})$ phase (-877 meV/M), but higher than the Si doped $\alpha\text{-}(\text{Al}_{0.94}\text{Si}_{0.06})_{4.75}(\text{Fe}_{2/3}\text{Mn}_{1/3})$ (-939 meV/M). These results highlight the critical role of Si stabilization in driving the phase transition from $\text{Al}_6(\text{FeMn})$ to $\alpha\text{-Al}_{15}(\text{Fe}, \text{Mn})_3\text{Si}_2$.

C. Energetics of Si and Mn addition into $\theta\text{-Al}_{13}\text{Fe}_4$

A commonly accepted crystal structure of $\theta\text{-Al}_{13}\text{Fe}_4$, as determined by Grin, *et al.* using the single crystal diffraction method [39], will be

Table 2

Comparison between the measured lattice parameters of Fe-IMCs in this study and the literature reported.

Phase	a	b	c	Angle	
$\alpha\text{-Al}_{15}(\text{Fe}, \text{Mn})_3\text{Si}_2$ (Primary)	12.618			90°	This work, TEM
$\alpha\text{-Al}_{15}(\text{Fe}, \text{Mn})_3\text{Si}_2$ (Binary Eutectic)	12.27			90°	This work, TEM
$\alpha\text{-Al}_{15}(\text{Fe}, \text{Mn})_3\text{Si}_2$ (Ternary Eutectic)	12.7			90°	This work, TEM
$\alpha\text{-Al}_{15}(\text{Fe}, \text{Mn})_3\text{Si}_2$	12.56			90°	[37]
$\theta\text{-Al}_{13}\text{Fe}_4$	15.492	8.078	12.47	$\beta = 107.69^\circ$	[39]
$\alpha\text{-Al}$	4.12			90°	This work, TEM

Table 3

Calculated results for chosen compositions of the $\text{Al}_6(\text{Fe}, \text{Mn})$ and $\alpha\text{-}(\text{Al}, \text{Si})_{4.75}(\text{Fe}, \text{Mn})$ phases (lattice parameters and formation energies). The lengths of the a and b -axis are normalized to the primitive cell. a^0 and b^0 represent the nominated values. \bar{a} represents the average value.

Compound	lattice Parameters (Å)	ΔE (meV/M)	Remarks
$\text{Al}_6(\text{Fe}_{0.75}\text{Mn}_{0.25})$	$a = 7.46$ [26] (calc.) $b = 6.47$ $c = 8.78$	-926	Mn/Fe random distribution
$\text{Al}_6(\text{Fe}_{0.6875}\text{Mn}_{0.3125})$	$a^0 = 7.46$, This work (calc.) $b^0 = 6.46$, $c = 8.79$	-919	Replacing one Al by Si costs over 0.28 eV, indicating
$\text{Al}_6(\text{Fe}_{0.6667}\text{Mn}_{0.3333})$	-	-918	unlikeness at ambient
$\text{Al}_6(\text{Fe}_{0.50}\text{Mn}_{0.50})$	$a = 7.49$ [26] (calc.) $b = 6.47$ $c = 8.78$	-914	conditions.
$\alpha\text{-Al}_{4.75}(\text{Fe}_{2/3}\text{Mn}_{1/3})$	$\bar{a} = 12.64$	-877	Mn at Fe 1 sites
$\alpha\text{-}(\text{Al}_{0.94}\text{Si}_{0.06})_{4.75}(\text{Fe}_{2/3}\text{Mn}_{1/3})$	$\bar{a} = 12.60$ This work (calc.) $a = 13.03$ this work(exp.) $a = 12.56$ [37] (exp.)	-939	Mn at Fe 1 sites Si prefers at Al7, Al4 sites

utilized in this study to investigate the stability of the $\theta\text{-Al}_{13}\text{Fe}_4$ phase. Experimental results have demonstrated the incorporation of Si and Mn into the $\theta\text{-Al}_{13}\text{Fe}_4$ structure. This section will explore the compositional variations (Si and Mn) in the θ phase and the corresponding stability changes, as well as the phase transitions associated with these variations.

The formation energy of $\theta\text{-Al}_{13}(\text{Fe}_{0.90}\text{Mn}_{0.10})_4$ corresponding to the experimental composition, is approximately -0.920 meV/M [26]. This suggests that at the formation temperature (1000 K), Mn can replace Fe atoms, forming ternary $\theta\text{-Al}_{13}(\text{Fe}_{1-x}\text{Mn}_x)_4$ phase due to the kinetical factors [26]. Under Mn-poor conditions, θ -phase is more stable than the $\text{Al}_6(\text{Fe}, \text{Mn})$ [26]. However, when the Mn content in $\text{Al}_y(\text{Fe}_{1-x}\text{Mn}_x)$ exceeds 9 at%, $\text{Al}_6(\text{Fe}_{1-x}\text{Mn}_x)$ becomes more stable. This can be attributed to the effects of compositional segregation on phase selection. Therefore, the $\text{Al}_6(\text{Fe}, \text{Mn})$ phase is selected in Mn-rich regions, while the $\theta\text{-Al}_{13}\text{Fe}_4$ phase is favored in Mn-poor regions.

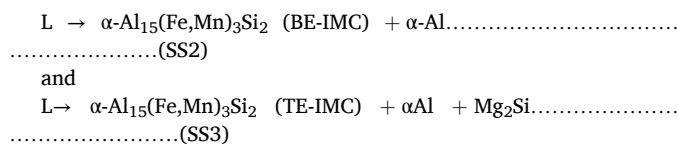
Additionally, the effect of Si incorporation on the stability variation of $\theta\text{-Al}_{13}\text{Fe}_4$ on was also investigated [21]. Si substitution at the Wyckoff 4i sites (Al9) enhances the stability of $\theta\text{-Al}_{13}\text{Fe}_4$. The formation energy of Si-doped $\theta\text{-Al}_{13}(\text{Fe}_{0.90}\text{Mn}_{0.10})_4$ structure is approximately -925 meV/M. This value is lower than that of $\text{Al}_6(\text{Fe}_{2/3}\text{Mn}_{1/3})$ (-0.918 eV/M), but higher than that of $\alpha\text{-}(\text{Al}_{0.94}\text{Si}_{0.06})_{4.75}(\text{Fe}_{2/3}\text{Mn}_{1/3})$ (-939 meV/M). In summary, the first-principles calculations established the following stability order (from low to high): $\alpha\text{-Al}_{4.75}(\text{Fe}_{2/3}\text{Mn}_{1/3}) < \text{Al}_6(\text{Fe}_{2/3}\text{Mn}_{1/3}) < \theta\text{-}(\text{Al}_{0.97}\text{Si}_{0.03})_{13}(\text{Fe}_{0.90}\text{Mn}_{0.10})_4 < \alpha\text{-}(\text{Al}_{0.94}\text{Si}_{0.06})_{4.75}(\text{Fe}_{2/3}\text{Mn}_{1/3})$. Si doping stabilizes both the θ - and α -phases. This stability relation aids in understanding the experimental observations.

4. Discussion

4.1. Phase competition among $\theta\text{-Al}_{13}\text{Fe}_4$, $\text{Al}_6(\text{Fe}, \text{Mn})$, and $\alpha\text{-Al}_{15}(\text{Fe}, \text{Mn})_3\text{Si}_2$

The solidification behaviour of the Al-5Mg-2Si-0.6Mn-1.3Fe alloy reveals a complex competition among Fe-IMCs, influenced by intrinsic and external factors. The phase diagram (Fig. 1) predicted that $\alpha\text{-Al}_{15}(\text{Fe}, \text{Mn})_3\text{Si}_2$ is the equilibrium primary phase due to its lowest formation energy among the Fe-IMCs. The calculated sequence involves solidification stages starting with primary $\alpha\text{-Al}_{15}(\text{Fe}, \text{Mn})_3\text{Si}_2$, followed by eutectic transformations producing $\alpha\text{-Al}_{15}(\text{Fe}, \text{Mn})_3\text{Si}_2$ and $\alpha\text{-Al}$, and ending with ternary eutectic transitions that include $\alpha\text{-Al}_{15}(\text{Fe}, \text{Mn})_3\text{Si}_2$, $\alpha\text{-Al}$, and Mg_2Si .

$L \rightarrow \alpha\text{-Al}_{15}(\text{Fe}, \text{Mn})_3\text{Si}_2$ (P-IMC).....
.....(SS1)



However, experiments demonstrate the prior formation of non-equilibrium phases, $\theta\text{-Al}_{13}\text{Fe}_4$ and $\text{Al}_6(\text{Fe},\text{Mn})$, which undergo transformations into equilibrium $\alpha\text{-Al}_{15}(\text{Fe},\text{Mn})_3\text{Si}_2$. This deviation highlights the significant role of various intrinsic and external influences.

Compositional differences among the Fe-IMCs which relative to the energetic stability play a critical role in the phase formation and phase transition competition. Experimental results (Fig. 10) reveal that $\theta\text{-Al}_{13}\text{Fe}_4$ contains moderate levels of Mn (~2.6 at%) and Si (~2.6 at%), while $\text{Al}_6(\text{Fe},\text{Mn})$ is Si-free with slightly higher Mn content (~4 at%). Conversely, $\alpha\text{-Al}_{15}(\text{Fe},\text{Mn})_3\text{Si}_2$ incorporates high levels of Si (~5.7 at%) and Mn (~4.6 at%). First-principles calculations show that Mn substitution for Fe and Si replacement of Al are energetically favourable for both $\theta\text{-Al}_{13}\text{Fe}_4$ and $\alpha\text{-Al}_{15}(\text{Fe},\text{Mn})_3\text{Si}_2$, enhancing their stability. The transformation mechanism from the Si-free $\text{Al}_6(\text{Fe},\text{Mn})$ to Si-rich phases such as $\alpha\text{-Al}_{15}(\text{Fe},\text{Mn})_3\text{Si}_2$ remains poorly understood. While $\text{Al}_6(\text{Fe},\text{Mn})$ is characterized by the absence of silicon within its crystal structure, the transition to Si-containing phases suggests a significant compositional and structural reorganization. The precise mechanisms driving the Si uptake and the atomic-scale dynamics of this transformation have yet to be fully elucidated, leaving a critical gap in understanding the evolution of Si-free to Si-rich phases in Fe-IMC systems.

The relationship between composition and crystal structure plays a critical role in determining phase formation and phase transformations of Fe-IMCs in aluminium alloys. The incorporation of alloying elements such as Si and Mn into each Fe-IMC affects their energetic preference for specific atomic sites, which in turn alters the lattice parameters along particular crystallographic axes [21,27]. This preferential substitution modifies the internal strain and symmetry within the crystal structure. As the lattice parameter variations approach critical thresholds, referred to as transition points, the crystal undergoes a structural transformation into a different type of Fe-IMC. $\theta\text{-Al}_{13}\text{Fe}_4$ has a monoclinic crystal structure (C 1 2/m 1 (12)) with lattice parameters of $a=15.492 \text{ \AA}$, $b=8.078 \text{ \AA}$, and $c=12.47 \text{ \AA}$ [39]. $\text{Al}_6(\text{Fe},\text{Mn})$ features an orthorhombic structure (Cmcm (63)), with $a=7.498 \text{ \AA}$, $b=6.495 \text{ \AA}$, and $c=8.837 \text{ \AA}$ [40]. In contrast, $\alpha\text{-Al}_{15}(\text{Fe},\text{Mn})_3\text{Si}_2$ has a body-centred cubic or simple cubic structure with a lattice parameter of $a=12.56 \text{ \AA}$ [37,38]. The phase transition between them is anticipated to be straightforward due to the similarity between the lattice parameters of θ and α phases. Specifically, the c -axis length of θ closely matches the a -axis length of α , while 1.5 times the b -axis length of θ aligns with the α lattice constant. Conversely, the transition from $\text{Al}_6(\text{Fe},\text{Mn})$ to α appears easier than $\text{Al}_6(\text{Fe},\text{Mn})$ to α due to their crystallographic compatibility. For instance, Si incorporation into $\theta\text{-Al}_{13}\text{Fe}_4$ replaces certain Al atoms, resulting in noticeable changes in the c -axis parameter, while Mn substitution similarly impacts the Fe lattice sites. Such compositional effects serve as key drivers for phase transitions between $\theta\text{-Al}_{13}\text{Fe}_4$, $\text{Al}_6(\text{Fe},\text{Mn})$, and $\alpha\text{-Al}_{15}(\text{Fe},\text{Mn})_3\text{Si}_2$, emphasizing the intricate relationship between alloying, lattice parameters, and crystal structure evolution. Further symmetry work are required to understand the complex relationship in variation between composition, lattice parameters and crystal structures.

The variation of the phase selection due to the phase competition at the SS1, resulted in the compositional variation within $\alpha\text{-Al}_{15}(\text{Fe},\text{Mn})_3\text{Si}_2$, as illustrated in Tables 1–2 and Fig. 11. During SS1, the equilibrium primary phase in the Al-5Mg-2Si-0.6Mn-1.3Fe alloy is predicted to incorporate the highest Mn and Si concentrations due to the abundance of these elements in the liquid melt. However, the observed Mn concentration (4.6 at%) and Si concentration (5.7 at%) in $\alpha\text{-Al}_{15}(\text{Fe},\text{Mn})_3\text{Si}_2$ were lower than the Mn (5.7 at%) and Si (6.3 at%) levels present in the binary eutectic. This discrepancy arises due to the formation of non-equilibrium phases, $\theta\text{-Al}_{13}\text{Fe}_4$ and $\text{Al}_6(\text{Fe},\text{Mn})$, which contain

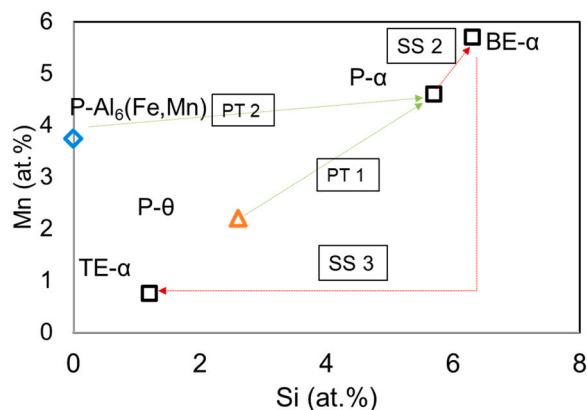


Fig. 11. Variation in Mn and Si concentrations across three types of Fe-IMCs, showing the compositional changes during solidification stages and phase transformation. Note: PT1 represents the phase transformation type 1, where $\theta\text{-Al}_{13}\text{Fe}_4$ transforms to $\alpha\text{-Al}_{15}(\text{Fe},\text{Mn})_3\text{Si}_2$, resulting in increased Si and Mn concentrations; PT2 represents the phase transformation type 2, where $\theta\text{-Al}_6(\text{Fe},\text{Mn})$ to $\alpha\text{-Al}_{15}(\text{Fe},\text{Mn})_3\text{Si}_2$, leading to a significant increase in Si and a slight rise of Mn concentration; SS2 refers to the second solidification stage (binary eutectic stage); and SS3 corresponds to the third solidification stage (ternary eutectic stage). The first solidification stage involves the formation of the primary Fe-IMCs.

significantly lower Mn and Si concentrations, thus depleting these elements before $\alpha\text{-Al}_{15}(\text{Fe},\text{Mn})_3\text{Si}_2$ solidification. Additionally, the reduced solubility of Mn and Si in aluminium at lower temperatures, especially at the binary eutectic, leads to the rejection of excess Mn and Si to the grain boundaries, resulting in localized enrichment in $\alpha\text{-Al}_{15}(\text{Fe},\text{Mn})_3\text{Si}_2$. Subsequently, during SS2 and SS3, as alloying elements are consumed, the $\alpha\text{-Al}_{15}(\text{Fe},\text{Mn})_3\text{Si}_2$ in the ternary eutectic solidifies with further diminished Mn and Si content.

The heterogeneous nucleation difficulty is one of the most important reasons that contributes to the phase selection of non-equilibrium Fe-IMCs. Without considering the incorporation of impurities or alloying elements, the basic constituting alloying elements of $\theta\text{-Al}_{13}\text{Fe}_4$, $\text{Al}_6(\text{Fe},\text{Mn})$, and $\alpha\text{-Al}_{15}(\text{Fe},\text{Mn})_3\text{Si}_2$ are Al and Fe, Al, Fe, and Mn, and Al, Fe, Mn, and Si, respectively. Heterogeneous nucleation of these Fe-IMCs requires different atomic species to occupy specific atomic positions, meaning that the more constituent elements involved, the more difficult the heterogeneous nucleation process becomes [12,14]. The experiments revealed a wide variety of Fe-IMC formations, which depend on casting conditions, particularly undercooling and cooling rates. It has been reported that the undercooling sequence for the heterogeneous nucleation of Fe-IMCs is: $\alpha\text{-Al}_{15}(\text{Fe},\text{Mn})_3\text{Si}_2 > \text{Al}_6(\text{Fe},\text{Mn}) > \theta\text{-Al}_{13}\text{Fe}_4$. Nucleation of $\alpha\text{-Al}_{15}(\text{Fe},\text{Mn})_3\text{Si}_2$ requires a relatively large undercooling, up to tens of Kelvin, while $\theta\text{-Al}_{13}\text{Fe}_4$ nucleates at undercoolings of less than 10 Kelvin [14]. The casting process, which typically involves high cooling rates (3.5 K/s in this study), is non-equilibrium, leading to complicated phase selection for Fe-IMCs. During the solidification process, the melt continues to cool before reaching the nucleation temperature of the equilibrium $\alpha\text{-Al}_{15}(\text{Fe},\text{Mn})_3\text{Si}_2$. As a result, other Fe-IMCs, such as $\text{Al}_6(\text{Fe},\text{Mn})$ and $\theta\text{-Al}_{13}\text{Fe}_4$, which require smaller nucleation undercoolings, have a higher likelihood of nucleating and growing. Theoretically, $\theta\text{-Al}_{13}\text{Fe}_4$ has a much higher chance of nucleating and remaining in the studied alloy as a non-equilibrium phase due to its significantly lower nucleation undercooling requirements.

The thermodynamic stability of these three different types of Fe-IMCs varies with changes in composition, particularly the concentration and incorporation of Mn and Si. The first-principles calculations in 3.4 demonstrated that the formation of $\text{Al}_6(\text{Fe},\text{Mn})$ is favoured in the Mn-rich area, while the formation of $\theta\text{-Al}_{13}\text{Fe}_4$ is preferred in the Mn-poor area. Si incorporation into these Fe-IMCs also plays a critical role in phase transitions. The segregation of Si on the surface of the Si-free

$\text{Al}_6(\text{Fe,Mn})$ phase promotes phase transitions towards the Si-favorable phases, $\theta\text{-Al}_{13}\text{Fe}_4$ and $\alpha\text{-Al}_{15}(\text{Fe,Mn})_3\text{Si}_2$.

Cooling rates also determine the spatial distribution of Fe-IMCs. $\theta\text{-Al}_{13}\text{Fe}_4$ primarily forms at the slower-cooled sample centre, while $\text{Al}_6(\text{Fe,Mn})$ nucleates at faster-cooled edges. Experimental results showed that $\theta\text{-Al}_{13}\text{Fe}_4$, which requires smaller nucleation undercooling, primarily forms at the centre of the sample where the cooling rate is lower. In contrast, $\text{Al}_6(\text{Fe,Mn})$, which requires a larger nucleation undercooling, predominantly forms at the edges of the sample where the cooling rate is higher. This observation indicates that higher cooling rates enhance the heterogeneous nucleation of Fe-IMCs requiring larger nucleation undercoolings. It is reported that [13], although under a very slow cooling rate, 0.01 K/s, the phase competition still existed. The non-equilibrium phase (mainly θ) was selected firstly and then transformed into equilibrium α .

Theoretically, $\theta\text{-Al}_{13}\text{Fe}_4$ has a higher likelihood of nucleating and persisting in Al-alloys as a non-equilibrium phase due to its significantly lower nucleation undercooling requirements. This behaviour has been supported by several studies [13,23,24]. However, experimental results (Fig. 2) demonstrated that the majority of $\text{Al}_6(\text{Fe,Mn})$ solidified at the edges of the sample, where cooling rates were higher. First-principles calculations further revealed that increased Mn concentrations stabilize $\text{Al}_6(\text{Fe,Mn})$, while Si stabilizes $\alpha\text{-Al}_{15}(\text{Fe,Mn})_3\text{Si}_2$. Thus, it can be inferred that the combined effects of higher Mn content, lower Si content, and higher cooling rates (at the sample edge) contributed to the formation of $\text{Al}_6(\text{Fe,Mn})$ in this study.

The presence of the selected non-equilibrium Fe-IMCs: $\text{Al}_6(\text{Fe,Mn})$ and $\theta\text{-Al}_{13}\text{Fe}_4$, becomes unstable as the temperature continues to decrease in the following solidification stages in the studied alloy. Consequently, further phase transformations occur. The mechanism of the phase transition between $\theta\text{-Al}_{13}\text{Fe}_4$ and $\alpha\text{-Al}_{15}(\text{Fe,Mn})_3\text{Si}_2$ has been thoroughly explained in previous work [13]. In this study, we focus on new observations of phase transformations between $\text{Al}_6(\text{Fe,Mn})/\theta$ and $\text{Al}_6(\text{Fe,Mn})/\alpha$, which will be discussed here.

4.2. Mechanism of phase transition from $\text{Al}_6(\text{Fe,Mn})$ (Si-free) to $\alpha\text{-Al}_{15}(\text{Fe,Mn})_3\text{Si}_2$ (high Si)

The phase transformation between $\text{Al}_6(\text{Fe,Mn})$ and $\alpha\text{-Al}_{15}(\text{Fe,Mn})_3\text{Si}_2$ is a diffusive process driven by changes in composition. This transformation aligns with most reported phase transitions among different Fe-IMCs, which are typically influenced by the diffusion of Si [23,24]. During the growth of primary $\text{Al}_6(\text{Fe,Mn})$, alloying elements in the liquid are rejected to the surface of the $\text{Al}_6(\text{Fe,Mn})$. Certain elements such as Si and Mg, which are not the constitute components, may accumulate at the surface of the $\text{Al}_6(\text{Fe,Mn})$. It has been reported that Mg segregation occurs at the surface of eutectic $\text{Al}_6(\text{Fe,Mn})$ in Al-1.4Fe-0.7Mn-xMg (x varied from 0.5 to 3.0 wt%) alloys [35]. Si, as an alloying element that cannot incorporate into $\text{Al}_6(\text{Fe,Mn})$, may also segregate at its surface. Experimental results have shown that $\text{Al}_6(\text{Fe,Mn})$ is unfavourable for both Mg and Si incorporation. However, there is a distinct difference between the segregation behaviours of Si and Mg, driven by their interactions with the $\text{Al}_6(\text{Fe,Mn})$ crystal. Si exhibits strong interactions with Fe and Mn, whereas Mg shows weak interactions with all atoms in $\text{Al}_6(\text{Fe,Mn})$. These interactions can be quantified by the heat of mixing values, which highlight the strength of bonding between different elements. The sequence of heat of mixing values for Si-Fe, Si-Mn, Si-Al, Mg-Fe, Mg-Mn, and Mg-Al is as follows: Si-Mn ($\Delta H_{\text{Si-Mn}}^{\text{mix}} = -45$ kJ/mol) > Si-Fe ($\Delta H_{\text{Si-Fe}}^{\text{mix}} = -35$ kJ/mol) > Si-Al ($\Delta H_{\text{Si-Al}}^{\text{mix}} = -19$ kJ/mol) > Mg-Al ($\Delta H_{\text{Mg-Al}}^{\text{mix}} = -2$ kJ/mol) > Mg-Mn ($\Delta H_{\text{Mg-Mn}}^{\text{mix}} = 10$ kJ/mol) > Mg-Fe ($\Delta H_{\text{Mg-Fe}}^{\text{mix}} = 18$ kJ/mol) [41]. This explains why the diffusion driving force for Si into $\text{Al}_6(\text{Fe,Mn})$ is greater than that for Mg. Another reason for the absence of observed Mg segregation on primary $\text{Al}_6(\text{Fe,Mn})$ in this study could be the higher formation temperature of primary $\text{Al}_6(\text{Fe,Mn})$ compared to the reported

binary eutectic $\text{Al}_6(\text{Fe,Mn})$ [35]. At higher temperatures, the solubility of Mg in liquid aluminium is increased, reducing the likelihood of Mg segregation during the solidification process.

The mechanism of this type of phase transformation is illustrated in Fig. 12. Following the formation of hollowed primary $\text{Al}_6(\text{Fe,Mn})$, Si becomes enriched at the surface of the $\text{Al}_6(\text{Fe,Mn})$. As the temperature decreases, $\text{Al}_6(\text{Fe,Mn})$ becomes thermodynamically unstable. This instability drives the diffusion of Si from surface segregation into the $\text{Al}_6(\text{Fe,Mn})$, a process that becomes energetic favourable. This diffusion triggers structural changes, where the incorporation of Si and the redistribution of Fe and Mn lead to Al atoms being rejected from the core into surrounding regions enriched with Si (Fig. 12b).

Consequently, the transformation of $\text{Al}_6(\text{Fe,Mn})$ to $\alpha\text{-Al}_{15}(\text{Fe,Mn})_3\text{Si}_2$ is accompanied by the formation of an $\alpha\text{-Al}$ phase. This results in a lamellar morphology between $\alpha\text{-Al}_{15}(\text{Fe,Mn})_3\text{Si}_2$ and $\alpha\text{-Al}$. Simultaneously, small amounts of Fe, Mn, and even Si remain in the transformed $\alpha\text{-Al}$, contributing to the subsequent formation of needle-like precipitates, as shown in Fig. 9c. $\text{Al}_6(\text{Fe,Mn})$ is a phase with zero tolerance for Si. The composition difference in Si concentration between $\text{Al}_6(\text{Fe,Mn})$ and $\alpha\text{-Al}_{15}(\text{Fe,Mn})_3\text{Si}_2$ is significant, reaching 5.7 at% (Table 1). This indicates that a high Si concentration is required for Si to incorporate into $\text{Al}_6(\text{Fe,Mn})$ before the formation of the new $\alpha\text{-Al}_{15}(\text{Fe,Mn})_3\text{Si}_2$ phase. Consequently, the phase transformation process between

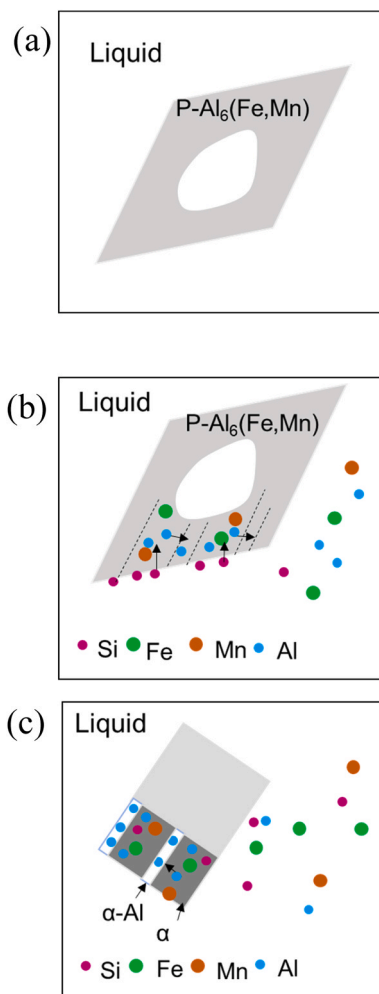


Fig. 12. Schematic diagram illustrating the phase transition mechanism of Liquid + $\text{Al}_6(\text{Fe,Mn}) \rightarrow \alpha\text{-Al}_{15}(\text{Fe,Mn})_3\text{Si}_2 + \alpha\text{-Al}$. (a) The hollowed structure of $\text{Al}_6(\text{Fe,Mn})$, (b) Si enrichment at the surface of $\text{Al}_6(\text{Fe,Mn})$, and (c) phase transformation from $\text{Al}_6(\text{Fe,Mn})$ to $\alpha\text{-Al}_{15}(\text{Fe,Mn})_3\text{Si}_2$, with the simultaneous precipitation of $\alpha\text{-Al}$ to compensate for the compositional difference.

$\text{Al}_6(\text{Fe},\text{Mn})$ and $\alpha\text{-Al}_{15}(\text{Fe},\text{Mn})_3\text{Si}_2$ is considered to be much slower than transformations involving phases with smaller compositional differences, such as $\text{Al}_{13}/\text{Al}_{15}$.

Phase transformations between $\text{Al}_6(\text{Fe},\text{Mn})$ and $\alpha\text{-Al}_{15}(\text{Fe},\text{Mn})_3\text{Si}_2$ observed in this study occurred without a specific orientation relationship, which can be attributed to several factors related to the nature of the phases and the transformation mechanisms. First, both $\text{Al}_6(\text{Fe},\text{Mn})$ and $\alpha\text{-Al}_{15}(\text{Fe},\text{Mn})_3\text{Si}_2$ have complex crystal structures. Transformations between phases with distinct and intricate structures often result in atomic arrangements that do not align in a manner that maintains a specific orientation relationship. Second, the transformation between $\text{Al}_6(\text{Fe},\text{Mn})$ and $\alpha\text{-Al}_{15}(\text{Fe},\text{Mn})_3\text{Si}_2$ is primarily driven by changes in thermodynamic stability rather than crystallographic constraints. In such cases, the emerging phase adopts a configuration that achieves stability, often without retaining any orientation relationship with the parent phase. Third, the lattice parameters of $\text{Al}_6(\text{Fe},\text{Mn})$ and $\alpha\text{-Al}_{15}(\text{Fe},\text{Mn})_3\text{Si}_2$ are significantly different. Maintaining a specific orientation under such conditions may be energetically unfavourable, further encouraging the formation of randomly oriented $\alpha\text{-Al}_{15}(\text{Fe},\text{Mn})_3\text{Si}_2$.

4.3. Mechanism of phase competition and transition between $\text{Al}_6(\text{Fe},\text{Mn})$ and $\theta\text{-Al}_{13}\text{Fe}_4$

It is well established that the Fe-IMCs exhibit excellent solubility for multiple alloying elements, typically Si and various 3d transition metals such as Mn, Cr, and others. The composition of the Fe-IMCs examined in this study (Table 1) indicate that $\theta\text{-Al}_{13}\text{Fe}_4$ incorporates both Si and Mn. However, only limited amounts of Si and Mn can be doped into $\theta\text{-Al}_{13}\text{Fe}_4$ without altering its crystal structure.

The experimental results demonstrated that both $\text{Al}_6(\text{Fe},\text{Mn})$ and $\theta\text{-Al}_{13}\text{Fe}_4$ are selected as primary phases in different regions of the sample during solidification process. The first-principles calculations conducted in this study provided crucial insights into the energetics and the role of Si stabilization in the formation of Fe-IMCs. The results indicate that the $\text{Al}_6(\text{Fe},\text{Mn})$ phase preferentially forms in Mn-rich areas, whereas $\theta\text{-Al}_{13}\text{Fe}_4$ phase is more likely to form in Mn-poor areas. The presence of Si enhances the formation capability of the $\theta\text{-Al}_{13}\text{Fe}_4$ phase. Previous first-principles calculations on the Mn/Fe alloying effects on the relative stability of $\text{Al}_6(\text{Fe},\text{Mn})$ and $\theta\text{-Al}_{13}\text{Fe}_4$ revealed that the θ -phase is more stable at low Mn content ($x < 0.08$). In contrast, the $\text{Al}_6(\text{Fe},\text{Mn})$ phase becomes more stable as Mn content increases ($x > 0.08$). This finding correlates with the observed formation of these two primary phases in regions with different Mn concentrations.

In this study, $\text{Al}_6(\text{Fe},\text{Mn})$ undergoes phase transformations into both $\theta\text{-Al}_{13}\text{Fe}_4$ and $\alpha\text{-Al}_{15}(\text{Fe},\text{Mn})_3\text{Si}_2$. The transformation from $\text{Al}_6(\text{Fe},\text{Mn})$ to $\alpha\text{-Al}_{15}(\text{Fe},\text{Mn})_3\text{Si}_2$ requires significantly higher Si concentrations and a slight increase in Fe and Mn, compared to the transformation into $\theta\text{-Al}_{13}\text{Fe}_4$. However, the diffusion of Si plays a more critical role in phase transformations among Fe-IMCs [23,24]. As a result, although $\alpha\text{-Al}_{15}(\text{Fe},\text{Mn})_3\text{Si}_2$ is the equilibrium phase in the studied alloy, regions with lower Si concentrations are more likely to favour the transformation from $\text{Al}_6(\text{Fe},\text{Mn})$ to $\theta\text{-Al}_{13}\text{Fe}_4$, as this requires less Si diffusion.

5. Summary

This study presents a novel perspective on the competitive interactions and phase transformations among multiple Fe-bearing intermetallic compounds (Fe-IMCs): $\theta\text{-Al}_{13}\text{Fe}_4$, $\text{Al}_6(\text{Fe},\text{Mn})$ and $\alpha\text{-Al}_{15}(\text{Fe},\text{Mn})_3\text{Si}_2$ in an Al-5Mg-2Si-0.6Mn-1.3Fe alloy cast at 700°C with a cooling rate of 3.5 K/s. It provides the first comprehensive observation of phase competition during both the liquid and solidification stages, emphasizing the influence of composition, nucleation dynamics, and cooling rates.

Key findings from this research include:

1. **Nucleation Competition:** The study reveals that heterogeneous nucleation competition occurs at temperatures higher than $\alpha\text{-Al}$ solidification. Non-equilibrium phases, such as $\theta\text{-Al}_{13}\text{Fe}_4$ and $\text{Al}_6(\text{Fe},\text{Mn})$, nucleate preferentially due to their lower nucleation barriers compared to the equilibrium $\alpha\text{-Al}_{15}(\text{Fe},\text{Mn})_3\text{Si}_2$ phase.
2. **Spatial Distribution of Phases:** $\theta\text{-Al}_{13}\text{Fe}_4$ forms in regions with slower cooling (e.g., the central part of the sample), while $\text{Al}_6(\text{Fe},\text{Mn})$ is more prevalent in faster-cooled regions (e.g., the sample edges).
3. **Phase Transformation Pathways:** Three distinct phase transformation mechanisms were identified during solidification:
 - $\text{Liquid} + \theta\text{-Al}_{13}\text{Fe}_4 \rightarrow \alpha\text{-Al}_{15}(\text{Fe},\text{Mn})_3\text{Si}_2 + \alpha\text{-Al}$ (irregular morphology): Fe diffusion out and Si diffusion in.
 - $\text{Liquid}(\text{Fe},\text{Si}) + \text{Al}_6(\text{Fe},\text{Mn}) \rightarrow \theta\text{-Al}_{13}\text{Fe}_4$: Fe and Si diffusion in with slight Mn diffusion out.
 - $\text{Liquid} + \text{Al}_6(\text{Fe},\text{Mn}) \rightarrow \alpha\text{-Al}_{15}(\text{Fe},\text{Mn})_3\text{Si}_2 + \alpha\text{-Al}$ (lamellar structure): Driven by Si diffusion in.
4. **Lamellar-Structure Formation:** The transformation from $\text{Al}_6(\text{Fe},\text{Mn})$ to $\alpha\text{-Al}_{15}(\text{Fe},\text{Mn})_3\text{Si}_2$ follows well-understood mechanisms, forming a distinctive lamellar structure. Notably, no clear orientation relationship was observed between $\text{Al}_6(\text{Fe},\text{Mn})$ and $\alpha\text{-Al}_{15}(\text{Fe},\text{Mn})_3\text{Si}_2$ in contrast to the $\theta\text{-Al}_{13}\text{Fe}_4$ to $\alpha\text{-Al}_{15}(\text{Fe},\text{Mn})_3\text{Si}_2$ transformation.
5. **Impact of Compositional Variations:** Si and Mn concentrations significantly influence phase formation, with higher Si $\alpha\text{-Al}_{15}(\text{Fe},\text{Mn})_3\text{Si}_2$ and higher Mn favouring $\text{Al}_6(\text{Fe},\text{Mn})$.

CRedit authorship contribution statement

Zhongyun Fan: Supervision, Funding acquisition. **Changming Fang:** Writing – review & editing, Investigation. **Zhongping Que:** Writing – review & editing, Writing – original draft, Visualization, Validation, Supervision, Software, Resources, Project administration, Methodology, Investigation, Funding acquisition, Formal analysis, Conceptualization.

Funding

This work was financial supported by the EPSRC (UK) for under grant number EP/N007638/1 (Future Liquid Metal Engineering Hub). Brunel University London BRIEF Award (11937131).

Declaration of Competing Interest

The authors declare that they have no known competing financial interests or personal relationships that could have appeared to influence the work reported in this paper.

References

- [1] UKRI Interdisciplinary Centre for Circular Metals, (<https://www.circularmetal.co.uk/>), 2025.
- [2] About BCAST- Sustainable Metallurgical Industry, (<https://www.brunel.ac.uk/research/Centres/BCAST/About-us>), 2025.
- [3] S.Vd Eynde, E. Bracquené, D. D-Romero, I. Zaplana, B. Engelen, J.R. Dufloy, J. R. Peeters, Forecasting global aluminium flows to demonstrate the need for improved sorting and recycling methods, Waste Manag. 137 (1) (2022) 231–240.
- [4] S. Al-Aliimi, N.K. Yusuf, A.M. Ghaleb, M.A. Lajis, S. Shamsudin, W. Zhou, Y. M. Altharan, H.S. Abdulwahab, Y. Saif, D.H. Didane, S.T.T. Ikhwan, A. Adam, Recycling aluminium for sustainable development: a review of different processing technologies in green manufacturing, Results Eng. 23 (2024) 102566.
- [5] D. Raabe, et al., Making sustainable aluminium by recycling scrap: the science of “dirty” alloys, Prog. Mater. Sci. 128 (2022) 100947.
- [6] G. Gaustad, E. Olivetti, R. Kirchain, Improving aluminium recycling: a survey of sorting and impurity removal technologies, Resour. Conserv. Recycl. 58 (2012) 79–87.
- [7] M.M.V. Fanconi, I.G. Fernández-Marcote, I. Ruiz-Bustanza, The challenge of impurities (Fe, Si) to recycling in the rolled aluminum industry in the coming years in relation to their influence on ultimate tensile strength, Metals 13 (12) (2023) 2014.

- [8] Y. Zhang, Y. Lei, Y. Ren, W. Ma, Removal of Fe impurities from Al alloy scraps by electromagnetic directional solidification combined with Si addition, *J. Mater. Res. Technol.* 26 (2023) 8738–8747.
- [9] Z. Que, Y. Wang, C.L. Mendis, C. Fang, J. Xia, X. Zhou, Z. Fan, Understanding Fe-containing intermetallic compounds in Al alloys: an overview of recent advances from the LiME research hub, *Metals* 12 (10) (2022) 1677.
- [10] S. Feng, Z. Jin, W. Du, I. Han, A. Lui, X. Zhou, P.R. Shearing, P.S. Grant, E. Liotti, The mechanism of Fe-rich intermetallic compound formation and growth on inoculants revealed by electron backscattered diffraction and X-ray imaging, *Mater. Des.* 232 (2023) 112110.
- [11] S. Patnaik, E. Ganju, X. Yu, M. Kang, J. Park, D.H. Kang, R. Kamat, J. Carsley, N. Chawla, Advancing sustainable aluminium alloy development via comprehensive 3D morphological and compositional characterization of Fe-rich intermetallic particles, *Metall. Mater. Trans. A* 55 (2024) 3762–3776.
- [12] Z. Que, Y. Wang, Z. Fan, T. Hashimoto, X.R. Zhou, Composition templating for heterogeneous nucleation of intermetallic compounds, *Sci. Rep.* 14 (1) (2024) 8968.
- [13] Z. Que, C.L. Mendis, Heterogeneous nucleation and phase transformation of Fe-rich intermetallic compounds in Al–Mg–Si alloys, *J. Alloy. Compd.* 836 (2020) 155515.
- [14] Z. Que, Y.P. Zhou, Y. Wang, Z. Fan, Composition templating for heterogeneous nucleation of intermetallic compounds, *Conf. Solidif. Process.* 17 (2017) 158–161.
- [15] Z. Que, Y. Wang, Z. Fan, T. Hashimoto, X. Zhou, Enhanced heterogeneous nucleation of $Al_6(Fe,Mn)$ compound in Al-alloys by interfacial segregation of Mn on TiB_2 particles surface, *Mater. Lett.* 323 (2022) 132570.
- [16] V. Stefanaiy, A. Griger, T. Turmezey, Intermetallic phases in the aluminium-side corner of the AlFeSi-alloy system, *J. Mater. Sci.* 22 (1987) 539–546.
- [17] S. Belmares-Perales, M. Castro-Roman, M. Herrera-Trejo, L.E. Ramirez-Vidauri, Effect of cooling rate and Fe/Mn weight ratio on volume fraction of α -AlFeSi and β -AlFeSi phases in Al-7.3Si-3.5Cu alloy, *Met. Mater. Int.* 41 (3) (2008) 307–314.
- [18] P. Popčević, et al., Anisotropic physical properties of the $Al_{13}Fe_4$ complex intermetallic and its ternary derivative $Al_{13}(Fe,Ni)_4$, *Phys. Rev. B* 81 (2010) 184203.
- [19] Y. Yang, S.Y. Zhong, Z. Chen, M. Wang, N. Ma, H. Wang, Effect of Cr content and heat-treatment on the high temperature strength of eutectic Al–Si alloys, *J. Alloy. Compd.* 647 (2015) 63–69.
- [20] N. Pang, Z. Shi, C. Wang, N. Li, Y. Lin, Influence of Cr, Mn, Co and Ni addition on crystallization behavior of $Al_{13}Fe_4$ phase in Al-5Fe alloys based on thermodynamic calculations, *Materials* 14 (4) (2021) 768.
- [21] C.M. Fang, Z. Que, A. Dinsdale, Z. Fan, Si Solution in θ - $Al_{13}Fe_4$ from First-principles, *Intermetallics*, 126 (2020) 106939.
- [22] Z. Que, C. Fang, J. Xia, Z. Fan, Influences of Zr and V addition on the crystal chemistry of θ - $Al_{13}Fe_4$ and the grain refinement of α -Al in an Al-4Fe alloy based on experiment and first-principle calculations, *Crystals* 14 (10) (2024) 879.
- [23] Z. Que, C. Fang, C.L. Mendis, Y. Wang, Z. Fan, Effects of Si solution in θ - $Al_{13}Fe_4$ on phase transformation between Fe-containing intermetallic compounds in Al alloys, *J. Alloy. Compd.* 932 (2023) 167587.
- [24] Z. Que, C.L. Mendis, Formation of θ - $Al_{13}Fe_4$ and the multi-step phase transformations to α - Al_8Fe_2Si , β - Al_5FeSi and δ - Al_4FeSi_2 in Al–20Si–0.7 Fe alloy, *Intermetallics* 127 (2020) 106960.
- [25] X. Huang, C. Gao, Z.S. Liu, K. Ma, X.C. Shi, G.Q. Wu, W.K. Xu, P.Z. Zhao, Y. Ma, Evolution of Fe-bearing phases during the fabrication and its effect on the mechanical properties of AA8014 aluminum alloy, *Mater. Today Commun.* 38 (2024) 108482.
- [26] A. Dinsdale, C.M. Fang, Z.P. Que, Z. Fan, Understanding the thermodynamics and crystal structure of complex Fe containing intermetallic phases formed on solidification of aluminium alloys, *JOM* 71 (2019) 1731–1736.
- [27] C.M. Fang, Z.P. Que, Z. Fan, Crystal chemistry and electronic structure of the β -AlFeSi phase from first-principles, *J. Solid State Chem.* 299 (2021) 122199.
- [28] D.C. Ma, Elastic properties of Mn-rich α intermetallic phase in engineering aluminum alloy: an ab initio study, *J. Appl. Phys.* 124 (2018) 085109.
- [29] Pandat, version 2021, database: Panaluminum. (<https://computherm.com/panaluminum/>).
- [30] E. Scheil, Bemerkungen zur Schichtkristallbildung, *Z. Met.* 34 (1942) 70–72.
- [31] Aluminium Association: Standard Test Procedure for Aluminium Alloy Grain Refiners: TP-1, Washington DC., 1987.
- [32] G. Kresse, J. Hafner, Ab initio molecular-dynamics simulation of the liquid-metal-amorphous-semiconductor transition in germanium, *Phys. Rev. B* 49 (1994) 14251–14269.
- [33] P.E. Blöchl, Projector augmented-wave method, *Phys. Rev. B* 50 (1994) 17953–17978.
- [34] J.P. Perdew, K. Burke, M. Ernzerhof, Generalized gradient approximation made simple, *Phys. Rev. Lett.* 77 (1996) 3865–3868.
- [35] Z. Que, Y. Zhou, Y. Wang, C.L. Mendis, Z. Fan, Effects of Mg addition on the Al6 (Fe, Mn) intermetallic compounds and the grain refinement of α -Al in Al-Fe-Mn alloys, *Mater. Charact.* 171 (2021) 110758.
- [36] Z. Que, Y. Wang, Z. Fan, Formation of the Fe-containing intermetallic compounds during solidification of Al-5Mg-2Si-0.7Mn-1.1Fe alloy, *Metall. Mater. Trans. A Phys. Metall. Mater. Sci.* 49 (6) (2018) 2173–2181.
- [37] M. Cooper, The crystal structure of the ternary alloy α (AlFeSi), *Acta Cryst.* 23 (6) (1967) 1106–1107.
- [38] M. Cooper, K. Robinson, The crystal structure of the ternary alloy α (AlMnSi), *Acta Cryst.* 20 (1966) 614.
- [39] J. Grin, U. Burkhard, M. Ellner, K. Peters, Refinement of the Fe_4Al_{13} structure and its relationship to the quasihomological homeotypical structures, *Z. Krist.* 209 (1994) 479–487.
- [40] J.G. Barlock, L.F. Mondolfo, Structure of some aluminium-iron-magnesium-manganese-silicon alloys, *Int. J. Mater. Res.* 66 (1975) 605.
- [41] A. Takeuchi, A. Inoue, Classification of bulk metallic glasses by atomic size difference, heat of mixing and period of constituent elements and its application to characterization of the main alloying element, *Mater. Trans.* 46 (12) (2005) 2817–2829.